Xu *et al.*
*Chinese Journal of Mechanical Engineering* (2022) 35:123
https://doi.org/10.1186/s10033-022-00792-3

Chinese Journal of Mechanical Engineering

ORIGINAL ARTICLE

Open Access

# Kinematic, Workspace and Force Analysis of A Five-DOF Hybrid Manipulator R(2RPR)R/SP+RR

Yundou Xu[1,2,3], Fan Yang[1,3], Youen Mei[1,3], Dongsheng Zhang[4], Yulin Zhou[3] and Yongsheng Zhao[1,2,3*]

**Abstract**

In the present study, the over-constrained hybrid manipulator R(2RPR)R/SP+RR is considered as the research objective. In this paper, kinematics of the hybrid manipulator, including the forward and inverse position, are analyzed. Then, the workspace is checked based on the inverse position solution to evaluate whether the workspace of the hybrid manipulator meets the requirements, and the actual workspace of the hybrid robot is analyzed. After that, the force analysis of the over-constrained parallel mechanism is carried out, and an ADAMS-ANSYS rigid-flexible hybrid body model is established to verify the simulation. Based on the obtained results from the force analysis, the manipulator structure is designed. Then, the structure optimization is carried out to improve the robot stiffness. Finally, calibration and workspace verification experiments are performed on the prototype, cutting experiment of an S-shaped aluminum alloy workpiece is completed, and the experiment verifies the machining ability of the prototype. This work conducts kinematics, workspace, force analyses, structural optimization design and experiments on the over-constrained hybrid manipulator R(2RPR)R/SP+RR, providing design basis and technical support for the development of the novel hybrid manipulator in practical engineering.

**Keywords:** Hybrid manipulator, Over-constrained, Kinematic analysis, Stiffness analysis

## 1 Introduction

With the continuous acceleration of the modernization process, the complexity of specimens involved in high-end manufacturing such as parts of aircraft, automobiles and ships has increased rapidly [1]. Accordingly, requirements of positioning accuracy and machining flexibility have continuously increased in the past years.

The serial robot has large workspace and good flexibility, but it is limited in the machining field that requires high precision and rigidity of the robot body. Parallel robots have large rigidity and strong carrying capacity, but they have shortcomings, such as small working space and poor flexibility [2]. Hybrid robots, especially five-degree-of-freedom (DOF) serial-parallel hybrid robots, have the advantages of parallel and serial robots in terms of stiffness and workspace, respectively. Accordingly, hybrid robots have attracted many researchers and enterprises [3–5]. Many scholars have conducted in-depth research on the five-DOF hybrid robot. Based on the two-rotation-one-translation (2R1T) parallel mechanism [6–8], some machining robots with good application prospects, including Tricept hybrid robots [9, 10], Exechon hybrid machining center [11, 12], Sprint Z3 tool head [13], TriMule [14, 15] and TriVariant hybrid robots [16, 17], and other robots based on (PUS+R)/PRR/PR [18, 19], 2-UPR/RPU [20, 21], 2-RPU/UPR [22, 23], 2-RPS/SPR [24], and 2-RPU/UPR/RPR [25], have been developed so far.

Zhang et al. [26] proposed a five-DOF hybrid mechanism R(2RPR)R/SP+RR, wherein the intersection of two revolute axes of the serial part (AC swing head) of the

*Correspondence: yszhao@ysu.edu.cn

[1] Laboratory of Parallel Robot and Mechatronic System of Hebei Province, Yanshan University, Qinhuangdao 066004, China
Full list of author information is available at the end of the article

mechanism was located on the extension line of the SP limbs. Then, the kinematic analyses were performed in this regard. However, in the actual design of this manipulator, the intersection of two revolute axes of the serial part is located in the circumcircle center of the triangle formed by the moving platform, thereby complicating the kinematic analyses.

In order to resolve the abovementioned shortcoming, kinematics, workspace and force analyses are conducted in the present study based on a novel design. Then, the corresponding stiffness, workspace and other performance indices are analyzed. Finally, an experimental platform is constructed to evaluate the performance index and meet the expected requirements. It should be indicated that in the entire manuscript, the notations R, P, U and S stand for revolute, prismatic, universal and spherical joints, respectively.

## 2 Motion Principle and Kinematic Analysis

### 2.1 Motion Principle

Xu et al. [27, 28] present a novel design of the hybrid manipulator, and its parallel part is R(2RPR)R/SP mechanism (see Figure 1). Each limb of the parallel part consists of upper and lower links connected to the fixed and moving platforms, respectively. Moreover, $A_1a_1(A_2a_2)$ limb form a UPU structure. Two U joints on the same side of two limbs are connected to the moving or fixed platforms and the two axes are collinear. Meanwhile, these two limbs are also recorded as a composite limb R(2RPR)R. The limb $A_3a_3$ is of SP structure, and the axis of P joint is perpendicular to the plane of the moving platform. Different from the mechanism described in Ref. [26], the intersection of the two revolute axes of the serial part is not located on the extension line of the SP limb.

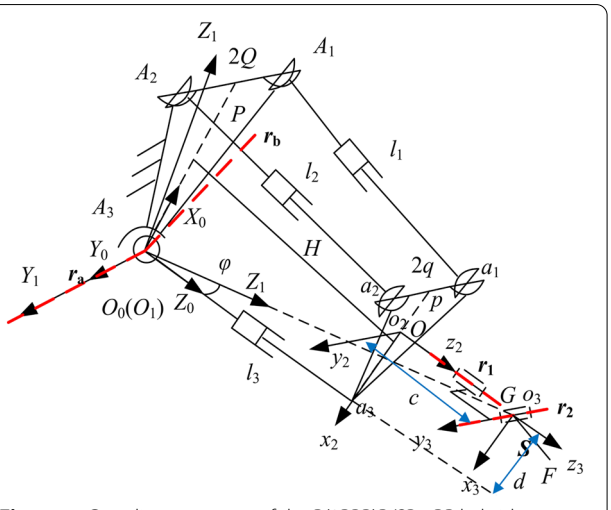


**Figure 1** Coordinate systems of the R(2RPR)R/SP+RR hybrid manipulator

### 2.2 Inverse Position Analysis

Figure 1 shows the coordinate system of the hybrid robot. It indicates that the origin of the reference coordinate $O_0$-$X_0Y_0Z_0$ is attached to point $A_3$ of the fixed platform, while the $X_0$-axis is perpendicular to the bottom side $A_1A_2$ and $Y_0$-axis is parallel to the bottom side $A_1A_2$. Moreover, the origin of the coordinate system $O_1$-$X_1Y_1Z_1$ is at point $A_3$, while the corresponding $Y_1$-axis is parallel to the bottom side $A_1A_2$ and the $Z_1$-axis coincides with vector $\boldsymbol{A_3G}$, where the point $G$ is the intersection of the two revolute axes of the serial part. The origin of the coordinate system $o_2$-$x_2y_2z_2$ is located at the connection between the AC swing head and the moving platform with the $z_2$- and $y_2$-axes coinciding with the C swing axis $\boldsymbol{r}_1$ and the A swing axis $\boldsymbol{r}_2$, respectively. The origin of the coordinate system $o_3$-$x_3y_3z_3$ is located at the intersection of the AC swing head, while the corresponding $z_3$-axis points to the tool tip point $F$ and the $y_3$-axis coincides with the A pendulum axis $\boldsymbol{r}_2$.

Given the coordinates of the proposed tool tip point $(x_F, y_F, z_F)^{\mathrm{T}}$ and the unit vector of the spindle head $\boldsymbol{S}$, the inverse position analysis is carried out to calculate the lengths $l_1$, $l_2$ and $l_3$ of the parallel mechanism and the angles $\psi_1$ and $\psi_2$ of the AC swing head. Then the coordinate of $a_i$ in the $O_1$-$X_1Y_1Z_1$ coordinate system can be obtained as the following:

$$\begin{cases} \boldsymbol{a}_1^1 = [\, pc\varphi - l_3s\varphi \;\; -q \;\; l_3c\varphi + ps\varphi \,], \\ \boldsymbol{a}_2^1 = [\, pc\varphi - l_3s\varphi \;\; q \;\; l_3c\varphi + ps\varphi \,], \\ \boldsymbol{a}_3^1 = [\, -l_3s\varphi \;\; 0 \;\; l_3c\varphi \,]. \end{cases} \tag{1}$$

Moreover, $\varphi$ is the angle between $Z_1$-axis and vector $\boldsymbol{A_3a_3}$. It should be indicated that in all calculations, the length of the bottom side of the moving platform triangle is $2q$ and the height is $p$. Based on Eq. (1), $\varphi$ can be expressed in the form below:

$$\varphi = \arcsin\left(\frac{p}{2L_G}\right), \tag{2}$$

where $L_G = \sqrt{x_G^2 + y_G^2 + z_G^2}$ is the length from the point $G$ to $O_0$, then

$$l_3 = \sqrt{L_G^2 - \left(\frac{p}{2}\right)^2} - k, \tag{3}$$

where $k$ is the distance between the intersection point $G$ of the AC head axes and the point $O$. The coordinate of the intersection point $G$ can be derived as follows:

$$\begin{cases} G_x = x_F - f[\,1\ 0\ 0\,]\boldsymbol{S}, \\ G_y = y_F - f[\,0\ 1\ 0\,]\boldsymbol{S}, \\ G_z = z_F - f[\,0\ 0\ 1\,]\boldsymbol{S}, \end{cases} \tag{4}$$

where $f$ is the distance from the tool tip to the point $G$, the orientation of the moving system $O_1$-$X_1Y_1Z_1$ relative to the reference coordinate system $O_0$-$X_0Y_0Z_0$ can be represented by a rotation matrix described by Euler angles $(\alpha, \beta, \gamma)$. This can be mathematically expressed in the form below:

$${}^0_1\boldsymbol{R} = \begin{bmatrix} \mathrm{c}\beta\mathrm{c}\gamma & -\mathrm{c}\beta\mathrm{s}\gamma & \mathrm{s}\beta \\ \mathrm{c}\alpha\mathrm{s}\gamma + \mathrm{c}\gamma\mathrm{s}\alpha\mathrm{s}\beta & \mathrm{c}\alpha\mathrm{c}\gamma - \mathrm{s}\alpha\mathrm{s}\beta\mathrm{s}\gamma & -\mathrm{c}\beta\mathrm{s}\alpha \\ \mathrm{s}\alpha\mathrm{s}\gamma - \mathrm{c}\alpha\mathrm{c}\gamma\mathrm{s}\beta & \mathrm{c}\gamma\mathrm{s}\alpha + \mathrm{c}\alpha\mathrm{s}\beta\mathrm{s}\gamma & \mathrm{c}\alpha\mathrm{c}\beta \end{bmatrix}, \tag{5}$$

where $\mathrm{s}\alpha$ and $\mathrm{c}\alpha$ denote $\sin\alpha$ and $\cos\alpha$, respectively. Moreover, the coordinate of point $G$ can be expressed as:

$$\begin{bmatrix} x_G \\ y_G \\ z_G \end{bmatrix} = {}^0_1\boldsymbol{R} \begin{bmatrix} 0 \\ 0 \\ L_G \end{bmatrix}. \tag{6}$$

Then,

$$\begin{cases} \alpha = \arctan\left(-\dfrac{y_G}{z_G}\right), \\ \beta = \arcsin\left(\dfrac{x_G}{L_G}\right). \end{cases} \tag{7}$$

According to the structural constraints of the mechanism, four points $A_1$, $A_2$, $a_1$, and $a_2$ are always in the same plane. Then the coupling angle $\gamma$ can be calculated from the following expression.

When $y_G = 0$,

$$\gamma = \arcsin\left(\frac{w}{\sqrt{u^2+v^2}}\right) - \arctan 2\left(\frac{v}{\sqrt{u^2+v^2}}, \frac{u}{\sqrt{u^2+v^2}}\right), \tag{8}$$

when $y_G \neq 0$,

$$\gamma = 2\arctan\left(\frac{u + \sqrt{u^2+v^2-w^2}}{v+w}\right), \tag{9}$$

$$\begin{cases} u = Pq\mathrm{c}\alpha\mathrm{s}\beta - q(L_G\mathrm{c}\varphi + p\mathrm{s}\varphi)\mathrm{c}\alpha, \\ v = Pq\mathrm{s}\alpha - q(L_G\mathrm{c}\varphi + p\mathrm{s}\varphi)\mathrm{c}\alpha\mathrm{s}\beta, \\ w = q(p\mathrm{c}\varphi - L_G\mathrm{s}\varphi)\mathrm{s}\alpha\mathrm{c}\beta, \end{cases} \tag{10}$$

where $P$ denotes the fixed platform triangle height. Subsequently, the length of the three branches of the parallel mechanism can be obtained from the following expression:

$$l_i = \left\| {}^0_1\boldsymbol{R}\boldsymbol{a}_i^1 - \boldsymbol{A}_i \right\|. \ (i = 1, 2, 3) \tag{11}$$

The rotation matrix of the coordinate system $o_3$-$x_3y_3z_3$ relative to the fixed coordinate system can be expressed as:

$$\boldsymbol{R} = {}^0_1\boldsymbol{R}\boldsymbol{R}_\varphi {}^1_2\boldsymbol{R}^2_3\boldsymbol{R}, \tag{12}$$

where $\boldsymbol{R}_\varphi$ is the rotation matrix respect to $\varphi$. Moreover, ${}^1_2\boldsymbol{R}$ and ${}^2_3\boldsymbol{R}$ denote the rotation matrices of the two rotation axes of the AC swing head, they can be obtained from the following expression:

$$\boldsymbol{R}_\varphi = \begin{bmatrix} -\mathrm{c}\varphi & 0 & \mathrm{s}(-\varphi) \\ 0 & 1 & 0 \\ -\mathrm{s}(-\varphi) & 0 & \mathrm{c}(-\varphi) \end{bmatrix}, \quad {}^1_2\boldsymbol{R} = \begin{bmatrix} \mathrm{c}\psi_1 & -\mathrm{s}\psi_1 & 0 \\ \mathrm{s}\psi_1 & \mathrm{c}\psi_1 & 0 \\ 0 & 0 & 1 \end{bmatrix},$$
$${}^2_3\boldsymbol{R} = \begin{bmatrix} \mathrm{c}\psi_2 & 0 & \mathrm{s}\psi_2 \\ 0 & 1 & 0 \\ -\mathrm{s}\psi_2 & 0 & \mathrm{c}\psi_2 \end{bmatrix}.$$

The unit vector of the spindle head can be expressed as:

$${}^0_1\boldsymbol{R}\boldsymbol{R}_\varphi {}^1_2\boldsymbol{R}^2_3\boldsymbol{R} \begin{bmatrix} 0 \\ 0 \\ 1 \end{bmatrix} = \boldsymbol{S}. \tag{13}$$

The two input angles of the AC swing head can be solved as the following:

$$\begin{cases} \psi_1 = \arctan\left(\dfrac{[\,0\ 1\ 0\,]\boldsymbol{R}_{\varphi 1}^{\mathrm{T}0}\boldsymbol{R}^{\mathrm{T}}\boldsymbol{S}}{[\,1\ 0\ 0\,]\boldsymbol{R}_{\varphi 1}^{\mathrm{T}0}\boldsymbol{R}^{\mathrm{T}}\boldsymbol{S}}\right), \\ \psi_2 = \arccos\left([\,0\ 0\ 1\,]\boldsymbol{R}_{\varphi 1}^{\mathrm{T}0}\boldsymbol{R}^{\mathrm{T}}\boldsymbol{S}\right). \end{cases} \tag{14}$$

Since the lengths $l_1$, $l_2$ and $l_3$ of the parallel part and the angles $\psi_1$ and $\psi_2$ of the AC swing head can be calculated from the foregoing expressions, the inverse position analysis of the robot is completed. It is worth noting that these parameters can be used for trajectory planning and workspace calculation.

### 2.3 Forward Position Analysis

In the forward position analysis, the lengths of three limbs of the parallel part (i.e., $l_1$, $l_2$ and $l_3$) and the two input angles of the AC swing head (i.e., $\psi_1$ and $\psi_2$) are known values. Accordingly, the main purpose of this analysis is to solve the coordinate of the tool tip point $F$ and the unit vector of the spindle head $\boldsymbol{S}$.

The orientation of the moving platform coordinate system $O_1$-$X_1Y_1Z_1$ relative to the fixed platform coordinate system $O_0$-$X_0Y_0Z_0$ can be described by the rotation matrix ${}^0_1\boldsymbol{R}$. The position of point $a_i$ on the moving platform in the coordinate system $O_0$-$X_0Y_0Z_0$ can be expressed in the form below:

$$\begin{cases} \boldsymbol{a}_1^0 = {}_1^0\boldsymbol{R}\boldsymbol{a}_1^1, \\ \boldsymbol{a}_2^0 = {}_1^0\boldsymbol{R}\boldsymbol{a}_2^1, \\ \boldsymbol{a}_3^0 = {}_1^0\boldsymbol{R}\boldsymbol{a}_3^1. \end{cases} \tag{15}$$

The expression $l_i = \left\|\boldsymbol{a}_i^0 - \boldsymbol{A}_i\right\| (i=1,\ 2,\ 3)$ is a system of ternary higher order equations. In the present study, 'Fsolve' function of MATLAB software was applied to calculate three rotation angles $\alpha$, $\beta$, $\gamma$ in ${}_1^0\boldsymbol{R}$. The position of the point $G$ in the coordinate system $O_1$-$X_1Y_1Z_1$ of the moving platform can be expressed as follows:

$${}^1\boldsymbol{G} = \begin{pmatrix} 0 & 0 & l_4 \end{pmatrix}^{\mathrm{T}}, \tag{16}$$

where $l_4$ is the length from point $A_3$ to point $G$ and

$$l_4 = \sqrt{(l_3 + k)^2 + \frac{p^2}{4}}.$$

Meanwhile, the position of the point $G$ in the fixed platform coordinate system $O_0$-$X_0Y_0Z_0$ can be obtained as the following:

$$\boldsymbol{G} = {}_1^0\boldsymbol{R}^1\boldsymbol{G} = \begin{pmatrix} x_G & y_G & z_G \end{pmatrix}^{\mathrm{T}}. \tag{17}$$

The rotation matrix $\boldsymbol{R}$ of the end coordinate system of the mechanism can be expressed as:

$$\boldsymbol{R} = {}_1^0\boldsymbol{R}\boldsymbol{R}_{\varphi}{}_2^1\boldsymbol{R}_3^2\boldsymbol{R}. \tag{18}$$

Based on the foregoing expressions, the unit vector of the spindle head $\boldsymbol{S}$ can be derived in the form below:

$$\boldsymbol{Q} = F\left(L_0,\ \theta - \theta_x,\ \frac{r}{R}\right). \tag{19}$$

Moreover, the coordinates of the tool tip point $F$ are obtained as:

$$\boldsymbol{S} = {}_1^0\boldsymbol{R}\boldsymbol{R}_{\varphi}{}_2^1\boldsymbol{R}_3^2\boldsymbol{R}\begin{bmatrix} 0 \\ 0 \\ 1 \end{bmatrix}. \tag{20}$$

The coordinate vector $\boldsymbol{F} = \begin{pmatrix} x_F & y_F & z_F \end{pmatrix}^{\mathrm{T}}$ of the tool tip point and the unit vector of the spindle head $\boldsymbol{S}$ can be obtained, which can be used for real-time detection of the machining process.

## 3 Workspace Analysis

### 3.1 Workspace Check

According to the performed manipulator kinematics analysis, the workspace of the manipulator can be searched based on the inverse position analysis. However, it is necessary to check whether the workspace represented by the intersection of the two rotation axes of the AC swing head meets the size of a ϕ1300 mm × 300 mm cylinder.

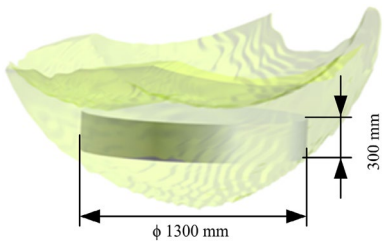


**Figure 2** Workspace appearance

In this regard, a large enough space containing the expected workspace [24] is considered at the first step. Then the points in the predetermined three-dimensional space are transformed into the inverse position solution of the mechanism, and the driving values of the mechanism are obtained to determine whether it is inside or outside the workspace. In the former case, the transformed point is printed, while in the latter case, the next point is selected to judge until all points in the space are searched. Finally, all points that meet the mechanism constraints are imported into the computational domain to form a three-dimensional appearance of the workspace, as shown in Figure 2.

Figure 2 indicates that the size of the manipulator's workspace can cover a ϕ1300 mm × 300 mm cylinder, which meets the requirements of the expected workspace.

### 3.2 Actual Workspace

In the practical working condition, the center of the end face of the AC swing head $F$, i.e., the tool tip point, where the tool holder is installed, is normally considered as the workspace reference point. It should be indicated that there are certain requirements for the angle ranges of the A- and C-axes of the AC swing head. The angle ranges of the A- and C-axes at the AC swing head are set to be ±40°, the actual effective stroke of each limb is 800 mm, the effective rotation range of the R joint is ±30°, and the rotation range of the S joint is ±35°. Since the solution of the actual workspace is similar to the presented analysis based on the inverse kinematics solution, the actual workspace can be solved by increasing the constraints of angle limits of the AC swing head. The actual size of structure parameters of the hybrid manipulator is shown in Table 1, based on which the workspace of the hybrid manipulator is solved.

Figure 3 shows the actual workspace of the five-DOF hybrid manipulator in the MATLAB environment. The

**Table 1** Size of structural parameters of the hybrid manipulator after optimization

| Parameter | Value (mm) |
|---|---|
| $2Q$ | 960 |
| $2q$ | 414 |
| $P$ | 835 |
| $p$ | 376 |
| $c$ | 429 |
| $d$ | 178 |
| $H$ | 1160 |

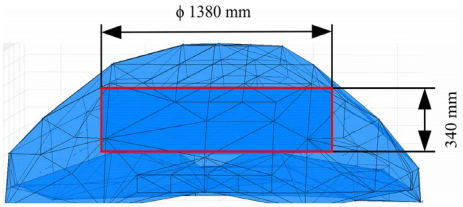


**Figure 3** Appearance of the real workspace

height of the actual workspace is 800 mm, the overall shape is similar to a mushroom, the head is convex, the bottom is concave, the middle part is relatively sharp and thick, and the surrounding boundary is blunt and thin.

It is worth noting that considering the small size of the head and bottom, an effective workspace cannot be formed. As a result, the workspace is concentrated in the middle. Meanwhile, the actual workspace is much larger than the planning workspace, which can meet the processing requirements.

In the present study, a ϕ1380 mm × 340 mm cylinder is considered as the actual workspace. It is observed that the size of the manipulator's actual workspace is larger than the positional workspace. It can completely include a ϕ1300 mm × 300 mm cylinder, which exceeds the requirement workspace.

## 4 Force Analysis and Structural Optimization Design

### 4.1 Force Analysis and Simulation Verification

In order to provide a theoretical basis for the structural design of the hybrid manipulator, force analysis should be carried out. On the other hand, the parallel mechanism of the manipulator R(2RPR)R/SP contains over-constraints, which generate static indeterminate problems in the force analysis. In order to resolve this problem, the weighted generalized inverse method [29, 30] is applied in the present study. Then the analytical solution of the force analysis of the over-constrained parallel mechanisms can be expressed as follows:

$$\boldsymbol{f} = \boldsymbol{W}^{-1}\left(\boldsymbol{G}_f^F\right)^{\mathrm{T}}\left(\boldsymbol{G}_f^F\boldsymbol{W}^{-1}\left(\boldsymbol{G}_f^F\right)^{\mathrm{T}}\right)^{-1}\$_F, \tag{21}$$

where $\boldsymbol{G}_f^F = \left(\$_{a1}\ \$_1^r\ \$_{a2}\ \$_2^r\ \$_{a3}\ \$_{31}^r\ \$_{32}^r\right)$ is the mapping matrix from $\boldsymbol{f}$ to $\$_F$, $\$_F$ denotes external forces exerted to the moving platform and $\boldsymbol{f} = \left(f_{a,1}\ m_{r,1}\ f_{a,2}\ m_{r,2}\ f_{a,3}\ f_{r,31}\ f_{r,32}\right)$ is the column vector composed of the magnitudes of the constraint and actuation wrenches. Moreover, $\boldsymbol{W}$ is the weighting matrix, composed of the stiffness of the constrained wrenches, which can be determined by the stiffness of each limb structure.

In the present study, it is assumed that limbs are cylindrical rods of equal cross-section, and the structural parameters are given as following Table 2.

**Table 2** The structural parameters

| Parameter | Value |
|---|---|
| $E$ (Pa) | $2.07 \times 10^{11}$ |
| $\mu$ | 0.29 |
| $H$ (m) | 0.335 |
| $2Q$ (m) | 0.3 |
| $2q$ (m) | 0.18 |
| $\theta_1$ | [−π/6~π/6] |
| $\theta_2$ | [−π/9~π/9] |
| $\$_F$ | (10 N 10 N 10 N; 10 N·m 10 N·m 10 N·m) |

In Table 2, $E$ represents the elastic modulus, $\mu$ represents the Poisson's ratio, $H$ represents the initial distance between the moving and fixed platforms, and $2Q$ and $2q$ represent the base length of the fixed and moving platforms triangle, respectively. The angles that the parallel mechanism rotates around the two rotational axes $\boldsymbol{r}_a$ and $\boldsymbol{r}_b$ [26] are $\theta_1$ and $\theta_2$, respectively. In the moving coordinate system $o$-$xyz$, the external load $\$_F$ is applied at the origin of the moving platform. Then constraint forces/couples and driving forces of each limb can be solved. Figures 4, 5, 6 present obtained results in this regard.

To evaluate the accuracy of the performed force analysis, the simulation model of the ADAMS-ANSYS rigid-flexible hybrid body is established, as shown in Figure 7. It is observed that in the coordinate system $o_2$-$x_2y_2z_2$, the above $\$_F$ is applied at the moving platform. For $t=0$–1 s, the moving platform has a trajectory $P(z) = 0.335 + 0.005t(m)$ along the $z_2$-direction. Moreover, the magnitude of each limb's driving force and

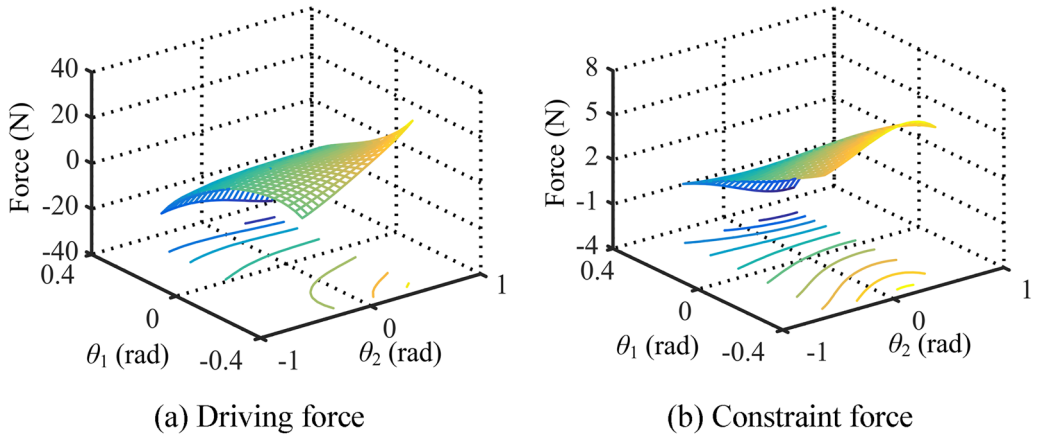


**Figure 4** Constraint wrenches distribution of the limb $U_{11}P_1U_{12}$

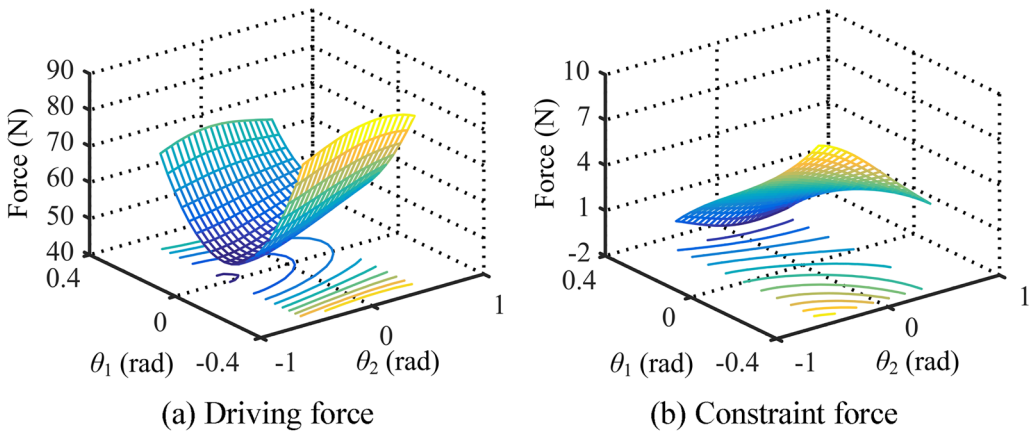


**Figure 5** Constraint wrenches distribution of the limb $U_{21}P_2U_{22}$

constraint forces/couples can be measured in the simulation model, and the results are shown in Figure 8.

When the mechanism is in the initial position (i.e., $t=0$ and $\alpha=\beta=0°$), the theoretical values of the magnitude of each limb's driving force, constraint forces/couples and the simulation ones are shown in Table 3.

In Table 3, the $D_f/C_f$ represents driving/constraint force, the $T_v/S_v$ represents theoretical/simulation value, the $A_e/R_e$ represents absolute/relative error. From Table 3, we know that the error between the theoretical and the simulation data is negligible, which proves the accuracy of the obtained results from the simulation and theoretical analysis. It is concluded that the performed analysis can be applied as the basis for subsequent manipulator design.

### 4.2 Structural Design Based on the Stiffness Optimization

Based on the force analysis and simulation results, the structure design of the five-DOF hybrid manipulator was completed, as shown in Figure 9. In the actual mechanism design process, specific structural forms and arrangements of components should be optimized. The objective of the structural optimization design is to improve the stiffness of the manipulator. And the ANSYS structure optimization module is used to analyze the deformation of the hybrid manipulator at each time the structural forms and sizes of key components were changed, and different configurations of the manipulator will be analyzed. While the milling force of 1000 N is applied at the tool tip along the *X*-, *Y*- and the axial direction respectively.

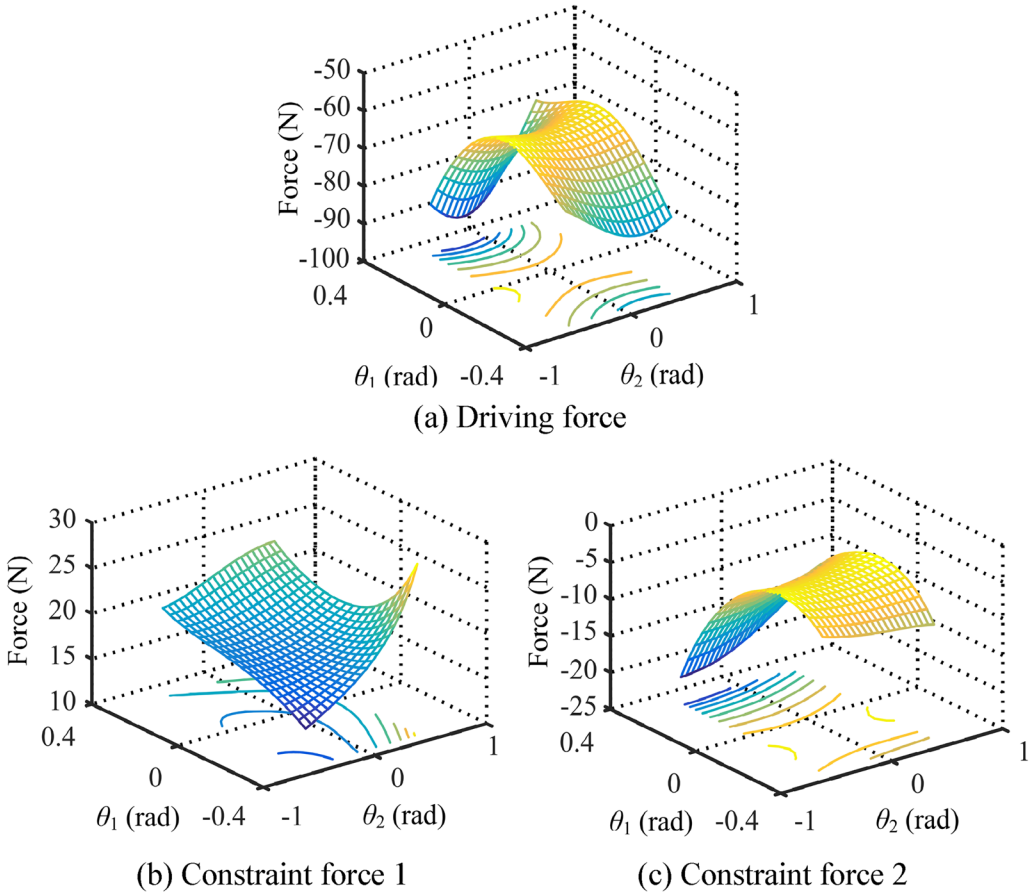


**Figure 6** Constraint wrenches distribution of the limb $S_3P_3$

Note that here only the situation that the milling force applied along the *X*-direction when the manipulator is in a specific configuration is analyzed before and after structural optimization, to demonstrate the effect of optimization.

In this regard, Figure 10 presents the deformation of manipulator originating from the applied load along the *X*-direction.

Accordingly, as shown in Figure 10, under the external load, the maximum deformation of each component of the hybrid manipulator can be obtained, and the weak area of the 3D model can be obtained. Thus, the structural forms and sizes of the weak area are improved step by step, the final 3D model of the optimized hybrid manipulator is shown in Figure 11.

And Figure 12 reveals that under the same loading condition as that in Figure 10, the maximum deformation of the end-effector of the optimized hybrid manipulator is 0.033891 mm and the calculated lateral stiffness increases from 22 N/μm to 29.5 N/μm, indicating that the hybrid manipulator has high stiffness and a good application prospect.

## 5 Prototype and Experiments

The prototype was manufactured based on the optimized 3D model, and the designed manipulator was calibrated by the laser tracker system (Figure 13).

First, the size of the workspace to reach the calculated size is verified. Let the end of the manipulator take a motion trajectory of a ϕ1300 mm circle and run it several times in the working space. The coordinates of the endpoints are captured by a laser tracker system. The distance between the nearest and the farthest trajectory is 330 mm. Moreover, when the manipulator moves to any point on the given trajectory, the length of each branch meets the design requirements and no alarms appeared on the branch limit switches. Consequently, it is concluded that the workspace meets the requirements.

After compensation based on calibration data, experimental results show that the average positioning accuracy

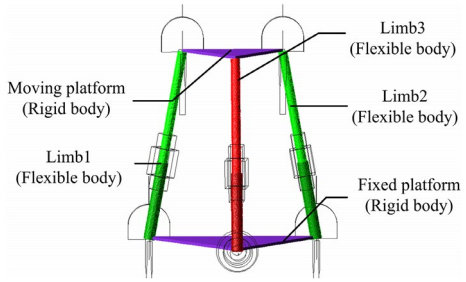


**Figure 7** Simulation model of the ADAMS-ANSYS rigid-flexible hybrid body

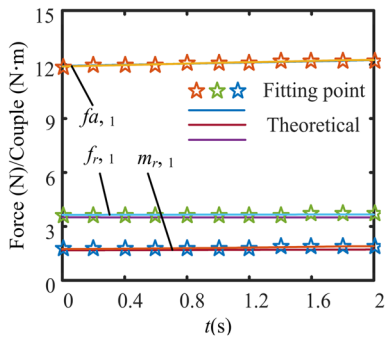


(a) $U_{11}P_1U_{12}$ limb1

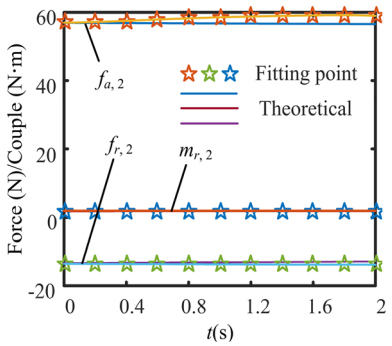


(b) $U_{21}P_2U_{22}$ limb2

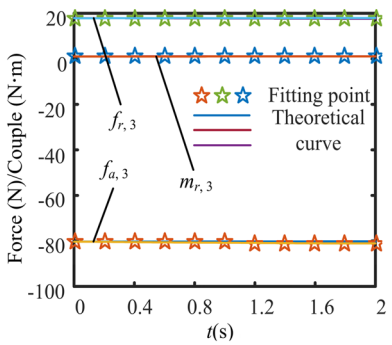


(c) $S_3P_3$ limb3

**Figure 8** Curves of the magnitude of constraint (driving) forces/couples

**Table 3** Theoretical and simulation values

| Limb | $D_f/C_f$ | $T_v$ | $S_v$ | $A_e$ | $R_e$ |
|---|---|---|---|---|---|
| Limb1 | $f_{a,1}$ | 4.0561 N | 3.981 N | 0.0751 | 1.85% |
| | $m_{r,1}$ | 3.0784 N·m | 3.182 N·m | −0.1036 | −3.37% |
| Limb2 | $f_{a,2}$ | 49.094 8N | 48.08 N | 1.0148 | 2.07% |
| | $m_{r,2}$ | 3.0784 N·m | 3.186 N·m | −0.1076 | −3.50% |
| Limb3 | $f_{a,3}$ | −62.8534 N | −62.66 N | −0.1934 | 0.31% |
| | $f_{r,31}$ | 17.9403 N | 18.35 N | −0.4097 | −2.28% |
| | $f_{r,32}$ | −5.7550 N | −5.87 N | 0.115 | −2.00% |

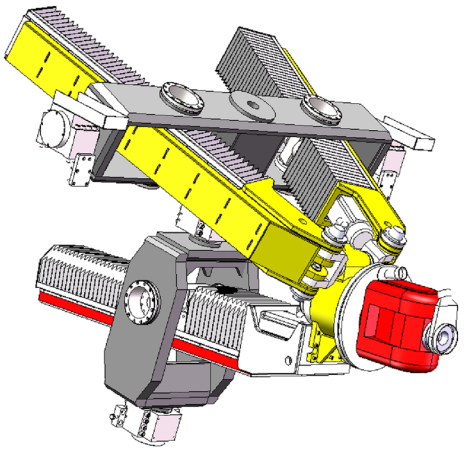

**Figure 9** 3D model of the hybrid manipulator

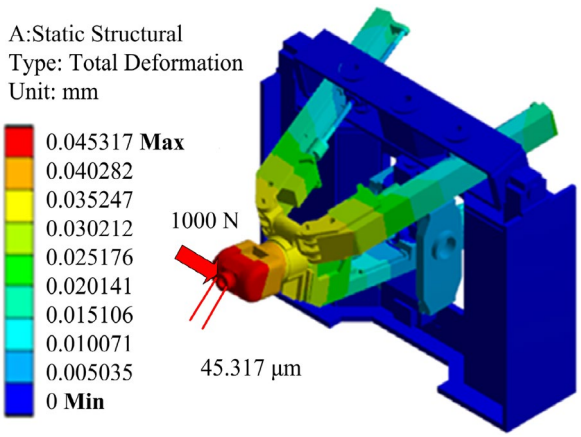


**Figure 10** Deformation of the manipulator originating from the applied load along the *X*-direction

along the *X*-, *Y*- and *Z*-directions are 0.0445, 0.0404 and 0.0164 mm, respectively [31, 32].

Then the re-position accuracy in four configurations, called $B_1$, $B_2$, $B_3$, and $B_4$ configurations, are measured. Let

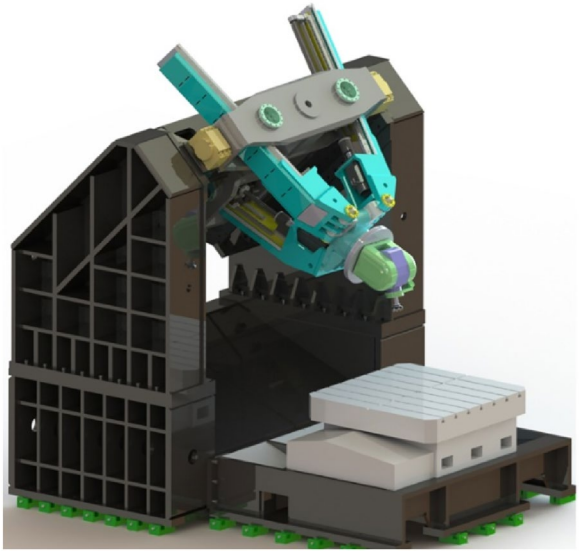

**Figure 11** 3D model of the optimized hybrid manipulator

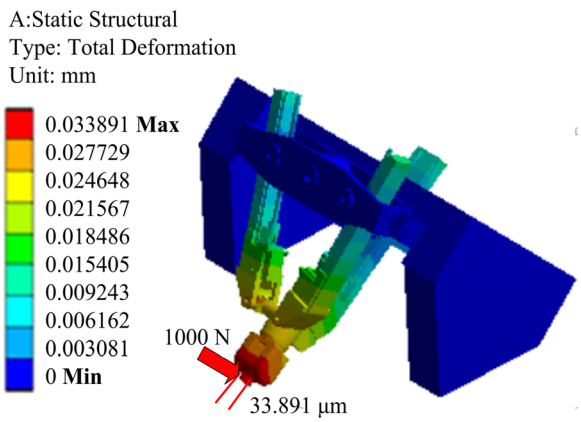


**Figure 12** Deformation of the optimized manipulator originating from the applied load along the *X*-direction

the manipulator start from the zero point and run to the farthest circular surface, then let the end of the manipulator take a motion trajectory of a ϕ1300 mm circle. The four intersection points of the circle and the $x$- and $y$-axes are taken as the repeatability measurement configurations, i.e., $B_1$, $B_2$, $B_3$ and $B_4$, which are shown in Figure 14. Position measurements of these four points are made by using a laser tracker system. Finally, the above processes are repeated 30 times to obtain the average value of the re-positioning accuracy of the manipulator at these four configurations, as shown in Table 4.

**Table 4** Re-position accuracy with different configurations (mm)

| $B_1$ | $B_2$ | $B_3$ | $B_4$ |
|---|---|---|---|
| 0.0164 | 0.0420 | 0.0461 | 0.0256 |

Finally, a milling experiment of an S-shaped aluminum alloy workpiece is planned to verify the machining ability of the hybrid manipulator prototype.

Figure 15a shows the cutting process moment of machining aluminum alloy components by the hybrid manipulator prototype. Figure 15b shows the S-shaped aluminum alloy workpiece processed by the prototype. The S-shaped workpiece exhibits a certain spatial surface with a good machining surface quality. It is concluded that the designed hybrid robot has good machining capabilities.

## 6 Conclusions

(1) In the present study, the intersection of the two rotation axes of the AC swing head is considered in the triangle formed by the moving platform, and the forward and inverse position of the five-DOF hybrid manipulator are solved for the hybrid mechanism R(2RPR)R/SP+RR. In particular, the analytical solution of the inverse position is derived. The presented solution is expected to become an important foundation for the subsequent motion control, parameter calibration and compensation. Then the robot's actual workspace that calculated with the tool tip point as the reference point is analyzed based on the kinematic calculation results, the calculation results show that it can meet the requirement workspace.

(2) Force analysis of the over-constrained parallel mechanism R(2RPR)R/SP is conducted by the weighted generalized inverse method, and an ADAMS-ANSYS rigid-flexible hybrid body model is applied to verify the simulation. Based on the finite element analysis results, the structure optimization design of the hybrid manipulator is completed and the manipulator stiffness is effectively improved.

(3) It is found that after the calibration, the positioning and re-position accuracy is greatly improved and meet the expected requirements. Meanwhile, the workspace of the endpoint of the prototype meets the expected requirements. The S-shaped workpiece machining concluded the designed hybrid robot has good machining capabilities.

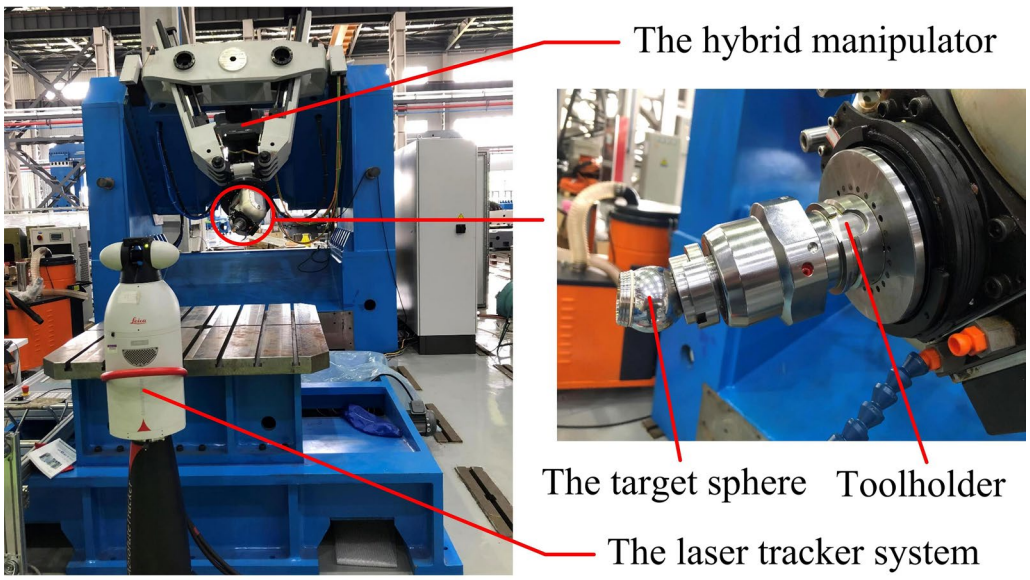


**Figure 13** Prototype of the 5-DOF hybrid manipulator

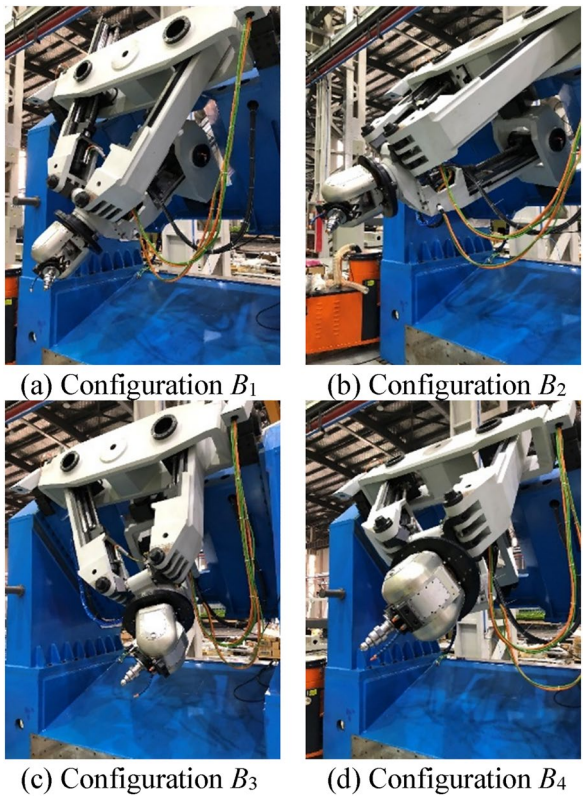


**Figure 14** Four configurations for measuring the re-position accuracy

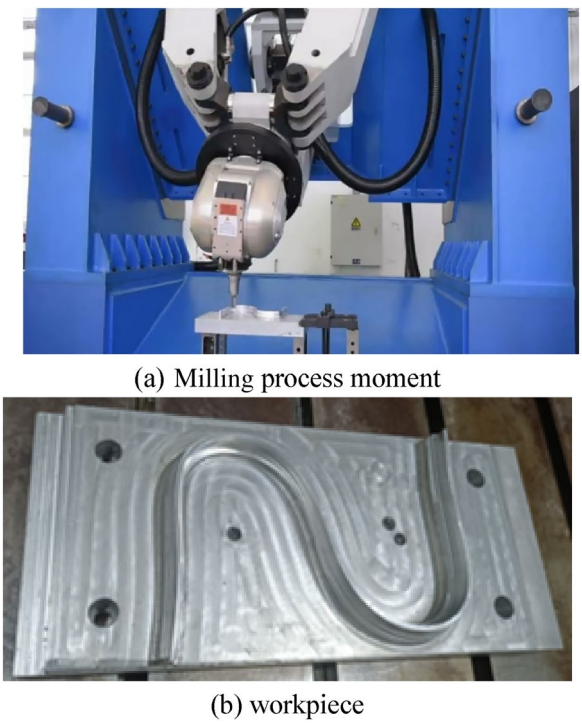


**Figure 15** Milling process and the workpiece

**Acknowledgements**
Not applicable.

**Authors' Contributions**
YSZ was responsible for the planning of the content and writing, YX analyzed the principle of design and force analysis, FY and YM performed the kinematic, workspace analysis, experimental analyses, DZ and YLZ were major contributors in writing the manuscript. All authors read and approved the final manuscript. All authors read and approved the final manuscript.

**Authors' Information**
Yundou Xu received the Ph.D. degree in Mechanical and Electronic Engineering from *Yanshan University, China*, in 2012. He is currently an associate professor at *School of Mechanical Engineering, Yanshan University, China*. His current research interests include parallel mechanisms and deployable mechanisms, and their application in the field of satellite antenna system, intelligent robots, etc.
Yang Fan is a master candidate at *Yanshan University, China*. His current research interests include parallel mechanisms and hybrid mechanisms, etc.
Youen Mei is a master candidate at *Yanshan University, China*. His current research interests include parallel mechanisms and hybrid mechanisms, etc.
Dongsheng Zhang received his Ph.D. degree in Mechanical and Electronic Engineering from *Yanshan University, China*. His current research interests include parallel mechanisms and hybrid mechanisms, etc.
Yulin Zhou received his Ph.D. degree in Mechanical Engineering from *Yanshan University, China*, in 2008. His current research interests include mechanisms, bionics and humanoid robots, etc.
Yongsheng Zhao received his Ph.D. degree in Mechanical Engineering from *Yanshan University, China*, in 1999. Since then, he has been a Professor with the *Robotics Research Center, Yanshan University, China*. His current research interests include parallel mechanisms, force and torque sensors, and advanced manufacturing technique.

**Funding**
Supported by National Natural Science Foundation of China (Grant No. 51875495), National Key R&D Program of China (Grant No. 2017YFB1301901), and Hebei Provincial Science and Technology Project of China (Grant No. 206Z1805G).

**Competing Interests**
The authors declare no competing financial interests.

**Author Details**
[1]Laboratory of Parallel Robot and Mechatronic System of Hebei Province, Yanshan University, Qinhuangdao 066004, China. [2]Key Laboratory of Advanced Forging & Stamping Technology and Science of Ministry of National Education, Yanshan University, Qinhuangdao 006004, China. [3]School of Mechanical Engineering, Yanshan University, Qinhuangdao 066004, China. [4]Tencent Robotics X, Tencent Holdings, Shenzhen 518057, China.

Received: 14 June 2021 Revised: 16 May 2022 Accepted: 5 August 2022
Published online: 30 September 2022

**References**

[1] Z X Zhou, T Y Zhou, Y H Ren. Current research and development trends of complex surface machining technology. *Journal of Mechanical Engineering*, 2010, 46(17): 105-113. (in Chinese)
[2] Y Jiang, T M Li, L P Wang, et al. Kinematic error modeling and identification of the over-constrained parallel kinematic machine. *Robotics and Computer-Integrated Manufacturing*, 2018, 49: 105-119.
[3] Z H Chong, F G Xie, X J Liu, et al. Design of the parallel mechanism for a hybrid mobile robot in wind turbine blades polishing. *Robotics and Computer-Integrated Manufacturing*, 2020, 61: 101857.
[4] W J Tian, M W Mou, J H Yang, et al. Kinematic calibration of a 5-DOF hybrid kinematic machine tool by considering the ill-posed identification problem using regularisation method. *Robotics and Computer-Integrated Manufacturing*, 2019, 60: 49-62.
[5] Y L Lai, C C Liao, Z G Chao. Inverse kinematics for a novel hybrid parallel–serial five-axis machine tool. *Robotics and Computer-Integrated Manufacturing*, 2018, 50: 63-79.
[6] T Sun, X Huo. Type synthesis of 1T2R parallel mechanisms with parasitic motions. *Mechanism and Machine Theory*, 2018, 128: 412-428.
[7] J Wei, J S Dai. Reconfiguration-aimed and manifold-operation based type synthesis of metamorphic parallel mechanisms with motion between 1R2T and 2R1T. *Mechanism and Machine Theory*, 2019, 139: 66-80.
[8] Y Song, P Han, P Wang. Type synthesis of 1T2R and 2R1T parallel mechanisms employing conformal geometric algebra. *Mechanism and Machine Theory*, 2018, 121: 475-486.
[9] F Caccavale, B Siciliano, L Villani. The Tricept robot: dynamics and impedance control. *Mechatronics IEEE/ASME Transactions on*, 2003, 8(2): 263-268.
[10] J L Olazagoitia, S Wyatt. New PKM Tricept T9000 and its application to flexible manufacturing at aerospace industry. *SAE Technical Papers*, 2007, 2007(2142): 37-48.
[11] Y Zhao, Y Jin, J Zhang. Kinetostatic modeling and analysis of an exechon parallel kinematic machine (PKM) module. *Chinese Journal of Mechanical Engineering*, 2016, 29(1): 33-44.
[12] Y Jin, Z M Bi, H T Liu, et al. Kinematic analysis and dimensional synthesis of exechon parallel kinematic machine for large volume machining. *Journal of Mechanisms & Robotics*, 2015, 7(4): 41004.
[13] T Sun, Y M Song. Dimensional synthesis of a 3-DOF parallel manipulator based on dimensionally homogeneous Jacobian matrix. *Sci. China Technol. Sc.*, 2010, 53(1): 168-174.
[14] T Huang, C Dong, H Liu, et al. A simple and visually orientated approach for type synthesis of overconstrained 1T2R parallel mechanisms. *Robotica*, 2019, 37(7): 1161-1173.
[15] T Huang, C Dong, H Liu, et al. Five-degree-of-freedom hybrid robot with rotational supports. US, Patent 9943967, 2017-4-27.
[16] M Li, T Huang, D G Chetwynd, et al. Forward position analysis of the 3-DOF module of the TriVariant: A 5-DOF reconfigurable hybrid robot. *Journal of Mechanical Design*, 2005, 128(1): 319-322.
[17] Y Y Wang, T Huang, X M Zhao, et al. Finite element analysis and comparison of two hybrid robots-The Tricept and the TriVariant. *IEEE International Conference on Intelligent Robots and Systems*, 2006: 490-495.
[18] Q Jin, T L Yang. Synthesis and analysis of a group of 3-degree-of-freedom partially decoupled parallel manipulators. *Journal of Mechanical Design*, 2004, 126(2): 301-306.
[19] F G Xie, X J Liu, J Wang. A 3DOF parallel manufacturing module and its kinematic optimization. *Robotics and Computer-Integrated Manufacturing*, 2012, 28(3): 334-343.
[20] Q Li, J M Herve. Type synthesis of 3-DOF RPR-equivalent parallel mechanisms. *IEEE T. Robot.*, 2014, 30(6): 1333-1343.
[21] L M Xu, X X Chai, Q C Li, et al. Design and experimental investigation of a new 2R1T overconstrained parallel kinematic machine with actuation redundancy. *Journal of Mechanisms and Robotics*, 2019, 11(3): 031016.
[22] D S Zhang, Y D Xu, J T Yao, et al. Analysis and optimization of a spatial parallel mechanism for a new 5-DOF hybrid serial-parallel manipulator. *Chinese Journal of Mechanical Engineering*, 2018, 31: 54.
[23] Y Xu, F Yang, Z Xu, et al. TriRhino: A five-DOF hybrid serial-parallel manipulator with all rotating axes being continuous: stiffness analysis and experiments. *Journal of Mechanisms and Robotics*, 2020, 13(2): 1-15.
[24] Y Xu, D S Zhang, J T Yao, et al. Type synthesis of the 2R1T parallel mechanism with two continuous rotational axes and study on the principle of its motion decoupling. *Mechanism and Machine Theory*, 2017, 108: 17-40.
[25] Y D Xu, Y Zhao, Y Yue, et al. Type synthesis of overconstrained 2R1T parallel mechanisms with the fewest kinematic joints based on the ultimate constraint wrenches. *Mechanism and Machine Theory*, 2020, 147: 103766.
[26] D Zhang, Y Xu, J Yao, et al. Design of a novel 5-DOF hybrid serial-parallel manipulator and theoretical analysis of its parallel part. *Robotics and Computer-Integrated Manufacturing*, 2018, 53: 228-239.
[27] Y Xu, Z Xu, F Yang, et al. Design and analysis of a new 5-DOF hybrid serial-parallel manipulator. *Mechanisms and Machine Science*, 2020, 79: 301-311.
[28] Y Xu, Z Xu, F Yang, et al. Design and analysis of a new 5-DOF hybrid robot considering workspace and force transmission efficiency. *China Mechanical Engineering*, 2019, 30(16): 1996-2002. (in Chinese)

[29] W Liu, Y Xu, J Yao, et al. The weighted Moore–Penrose generalized inverse and the force analysis of overconstrained parallel mechanisms. *Multibody System Dynamics*, 2016: 1-21.
[30] Y Xu, W Liu, J Yao, et al. A method for force analysis of the overconstrained lower mobility parallel mechanism. *Mechanism and Machine Theory*, 2015, 88: 31-48.
[31] H Ye, D Wang, J Wu, et al. Forward and inverse kinematics of a 5-DOF hybrid robot for composite material machining. *Robotics and Computer-Integrated Manufacturing*, 2020, 65: 101961.
[32] L Huang, L R Yin, B Liu, et al. Design and error evaluation of planar 2-DOF remote center of motion mechanisms with cable transmissions. *Journal of Mechanical Design*, 2021, 143(1): 013301.